A Coarse-Grained Molecular Model of Strain-Hardening for Polymers in the Marginally Glassy State

Kapileswar Nayak,[1] Daniel J. Read,[1] Tom C. B. McLeish,[2] Peter J. Hine,[3] Manlio Tassieri[3]

[1]School of Mathematics, University of Leeds, Leeds LS2 9JT, United Kingdom

[2]Department of Physics, University of Durham, Durham DH1 3HP, United Kingdom

[3]School of Physics and Astronomy, University of Leeds, Leeds LS2 9JT, United Kingdom

Correspondence to: D. Read (E-mail: d.j.read@leeds.ac.uk)

ABSTRACT: We have developed a simple bead-spring model, intended to mimic the internal dynamics of individual polymer chains in the region of the glass transition temperature. Entanglement constraints on the chains are approximated by "sliplinks." We model the chain dynamics using a dynamic Monte Carlo scheme, with a hop acceptance criterion based on the traversal of high energy barriers. We use this to address the recent experiments of Hine et al., which investigated the effects of melt processing on stress-strain behavior. Polystyrene samples were stretched, annealed at constant length for various times, then either subjected to shrinkage tests or further stress-strain tests. Our model reproduces, at a qualitative level, the observations of Hine et al. It indicates that whilst the initial (weak) strain hardening involves deformation of chain subunits smaller than the entanglement length, the transition to stronger strain hardening involves the "pulling tight" of a small fraction of chain strands trapped in between entanglements. The insights gained suggest a route towards development of molecular-based constitutive models for strain hardening in the glassy state, and specifically the effect of melt processing. © 2011 Wiley Periodicals, Inc. J Polym Sci Part B: Polym Phys 49: 920–938, 2011

KEYWORDS: drawing; glass; simulations; strain-hardening; stress

INTRODUCTION The typical stress-strain behavior of glassy polymers shows an initial yield stress at very small strain, followed by plastic flow and subsequent strain hardening at higher strain. There are several constitutive equations available[1–6] which successfully model the stress-strain behavior using a combination of springs and dashpot elements. The common feature of these models is the use of a nonlinear viscous dashpot in series with a stiff spring to describe the small strain elastic response, yield and plastic flow of the material; in parallel with this, a weaker nonlinear spring provides strain hardening at high strains. Successful as these models are, they do not attempt to understand the molecular origin of the strain hardening behavior of polymer glasses at a level beyond the motivational. Traditionally, and in the development of the above models, strain hardening behavior has been attributed to entanglements between polymer chains, assuming that the entanglements act as effective crosslink points, so leading to a neo-Hookean formulation for the hardening stress based on rubber elasticity theory. Although such constitutive models are quite successful in engineering applications, this explanation for the hardening stress has been questioned recently from a number of angles. The strain hardening modulus in glassy state is typically much larger than the melt plateau modulus and

decreases with increasing temperature.[7,8] It is also observed both by NMR[9] and SANS[10–12] that the polymer chains in the glassy state deform as if their apparent network density is significantly higher than the melt state (an observation which is backed up by recent computer simulation).[13–15] This, on its own, provides some explanation for the high hardening modulus: it indicates that the chains do not equilibrate on the entanglement lengthscale during glassy deformation, becoming stretched on smaller lengthscales, thus giving higher stresses. There may, additionally, be viscous contributions to the hardening stress, which will be discussed further below – this provides an alternative explanation for the high hardening modulus.

It is possible, then, that the strain hardening can be attributed simply to stretched and oriented chains (i.e., producing stress from an entropic origin and/or increases in internal chain energy) even though this may not be, primarily, a direct result of entanglements. There is some support for this from the computer simulations of Li et al.[16] and Chui and Boyce[17] where the contribution of different types of interatomic force to the sample stress are measured. They observe that, at small strain, bonded and nonbonded interactions both make significant contributions to the stress.

WILEY ONLINE LIBRARY

However, strain-hardening arises at large strain mainly due to the bonded interaction, which means the orientation and stretching of chains are mainly responsible for this effect.

There are, however, recent indications that glassy strain hardening may involve more than merely a direct contribution to stress from stretched chains. Strain hardening is observed to be strain-rate dependent, both in experiments[9] and in simulation,[14] leading to the inference that there may also be a viscous contribution to strain hardening. Additionally, Hoy and Robbins[13,14] showed in their molecular dynamics simulations that, at least at extremely low temperature, the dissipative contribution to the stress was directly proportional to the rate of plastic rearrangements and that this included most of the hardening stress. Although there is more than one way to interpret this observation (it would be quite surprising not to observe a strong correlation between rate of dissipation and rate of molecular rearrangements) this is certainly consistent with viscous contributions to strain hardening. Finally, Chen and Schweizer[18] have proposed a theory for strain hardening where the stress arises solely from intermolecular forces, through the influence on chain orientation on local packing and activation energy barriers. Still, if the strain hardening includes a viscous contribution, there seems to be agreement that this increase in viscosity is coupled to the chain configuration: that is, chain orientation and stretching are still key quantities. Moreover, there is support from simulations on deformation of binary blends[15] for the notion of stress superposition: each chain appears essentially to move in a glassy "mean field," and the stress contributions from long and short chains are additive.

Potentially differential scanning calorimetry (DSC) experiments (such as the ones performed by Hasan and Boyce[19]) could also shed light on the different contributions to the hardening stress. However, DSC is only able to reveal energy stored internally during the deformation process, and so it cannot distinguish between nonenergetic contributions to hardening (both entropic and viscous contributions are nonenergetic). Hasan and Boyce[19] observed an increase in the stored energy occurring during the strain hardening regime, but only as a relatively small fraction (ca. 10%) of the total work done against the hardening stress, implying that the majority of this stress came from a nonenergetic origin.

A better method for distinguishing elastic and viscous contributions to strain hardening comes through reverse-strain experiments. Recent experiments by Senden et al.,[20] involving tensile deformation followed by compression, suggest that a combination of viscous and elastic elements provides a more accurate description of strain hardening. Extensive simulations by Ge and Robbins[21] give qualitatively similar results (though with a weaker strain hardening, due to their simulation parameters) but these are not analysed in the same way as in Senden et al.[20]

Although strain hardening cannot solely be attributed to entanglements, there remains the question as to whether entanglements (from the melt state) retain some importance for strain hardening. This is closely related to the issue of how, and whether, strain hardening in the glassy state is influenced by processing in the molten state and also to the difficult challenge of constitutive modelling during cooling through the glass transition. To tackle these questions, it is important to understand the development of molecular structure and orientation from melt state to glassy state. It is well known that flow in the melt state can produce different levels of molecular orientation at different length scales.[22] Therefore, it is necessary to know that which length scales are important in describing the amorphous glass deformation. One might ultimately hope to be able to predict the level of molecular orientation induced by a given flow and given temperature history during the melt processing and their effect on the solid state deformation. Recent advances in our understanding of the entangled melt state[22–25] provide both working tools and an incentive to extend the molecular approach into the solid glassy phase.

Motivated by this programme, the experiments of Hine et al.,[26] investigated the effects of melt processing on stress-strain behavior. They used commercially available polydisperse polystyrene, which had an average molecular weight (Mw) of 270000 g/mol and polydispersity of 2.74 (this molecular weight corresponds to ∼2400 chemical monomer units, or 16–17 entanglement units). The polystyrene samples were stretched (up to a draw ratio 4:1 at 115 °C), annealed at constant length for various times (at 115 °C), then either subjected to shrinkage tests (at 125 °C) or further stress-strain tests (at the lower temperature of 105 °C). They made several observations: (i) on annealing, the sample birefringence begins to drop immediately, for times shorter than the chain entanglement time, but (ii) the sample shrinkage remains constant up to about three times the entanglement time, dropping with a characteristic annealing time-scale similar to the chain Rouse time, (iii) strain-hardening during subsequent deformation is reduced by even small amounts of annealing, and (iv) the strain-hardening curve appears to be correlated to sample shrinkage (defined as the amount by which a sample would shrink when heated above the glass transition temperature) such that curves for samples with the same shrinkage can be superposed by shifting along the strain axis. Hine et al. inferred that the initial (weak) strain hardening involves orientation and deformation of chain subunits much smaller than the entanglement length, but also that the transition to stronger strain hardening involved the "pulling tight" of chain strands in-between entanglements. On average (and in the absence of large scale chain relaxation) one expects chains between to "pull tight" at deformation ratios of order $2\sqrt{N_{ek}}$ where N_{ek} is the number of Kuhn segments between entanglements (the factor of 2 arises from the large-strain limit of the Doi-Edwards α parameter, eqn 7.139 of ref. 24). This limit is independent of overall molecular weight for well entangled systems, and gives a strain of order 12 for polystyrene. However, this is an estimate based on an "average" segment; one issue (to be addressed in this article) is whether the tails of the distribution are important for the limit of extension.

The work presented here is aimed at developing a simple computational implementation of a coarse-grained molecular model for deformation in this marginally-glassy regime, consistent with the NMR and SANS experiments above, to assess to what degree it reproduces the observations of Hine et al., and to investigate the inferences drawn. We shall also present results from an extension of their experiments to monodisperse polystyrene of average molecular weight of 260,000 g/mol (corresponding to ∼2300 chemical monomer units, or 15–16 entanglement units as used in refs. 22 and 23) taken through exactly the same experimental procedure as detailed in Hine et al.[26] The insights gained promise to assist the development of simplified constitutive models for strain hardening, addressing specifically the effect of melt processing.

COMPUTATIONAL METHODOLOGY

Bead Spring Model

We employ a coarse-grained bead-spring chain model, designed to represent the dynamics of individual chains, in the melt and marginally glassy state, at length scales corresponding to a small number of connected monomers and above. A single chain consists of $N+1$ coarse-grained beads connected by N springs with nonlinear spring forces (to capture the finite extensibility of the chain; this will be the underlying origin of strong strain-hardening in the glassy state of our model). Each "bead" in the model represents a small number of chemical monomers but does not contain any microscopic details (local chemical structure) of the polymer.

In the melt state, polymer chains are entangled with each other; this restricts the dynamics of the chains, giving rise to the characteristic melt rheological behavior. It is often conjectured that entanglements also affect the strain-hardening in the glassy state. To investigate the relationship between relaxations in the melt state during processing and strain hardening in the glassy state, and in particular the role of entanglements, we introduce the simplest possible model for entanglement effects: point-like slip-links which restrict the motion of the chains. In our model, the sliplinks are fixed at positions which deform affinely with the macroscopic strain (similar to refs. 27 and 28, but lacking the development of, for example, ref. 29 where sliplinks are attached to a fixed background via a confining spring, and so allowed to fluctuate ca. their average positions). This introduces a further parameter in the model, the average number of beads per slip-link.

It is worth a brief discussion of the limitations of sliplink-based simulation. Sliplink simulations offer an intermediate level of coarse-graining between computationally intensive molecular dynamics simulations[13–17,21] and analytical models. We aim to model the dynamics of individual chains based on a guess as to the underlying chain dynamics; comparison with experimental data and/or more detailed simulations can reveal whether these guessed dynamics are reasonable. But, because these models offer ready access to internal variables (such as entanglement dynamics) these can in turn inform and test the assumptions of analytical models (which is one reason for their use in melt-state rhe-
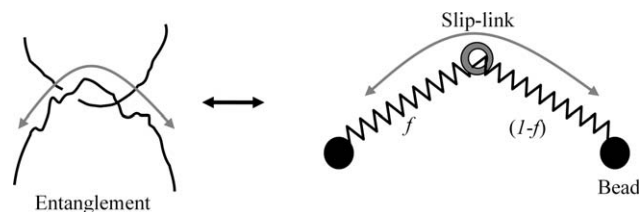
FIGURE 1 A sliplink splits the a spring to two subsprings, containing a fraction f and $(1-f)$ of the chain respectively. In our model, these springs are not colinear.

ology[27–29] and also our reason for using them here). An obvious limitation, with respect to the glassy state, is the neglect of intermolecular interactions. We shall attempt (see below) to take some account of the existence of large energy barriers towards polymer motion in terms of their effect on chain dynamics. We cannot, however, access the stress due to intermolecular interactions, which contribute to the yield and viscous flow stress (such stress contributions need to be added to those obtained in our model). In using this simulation to address the issue of strain hardening, we are assuming that strain hardening is dominated by intramolecular forces (or that any intermolecular viscous strain hardening contributions are proportional to the intramolecular ones). This is a strong assumption, which can be validated only through comparison with experiments, which is our intention here (it may also be that the assumption is reasonable in the marginally glassy state but becomes worse upon further cooling). Furthermore, we cannot use sliplink simulations to contribute directly to the debate surrounding viscous and elastic strain hardening contributions, although we will (in the conclusions) offer some indications as to how this model may yet retain some use within a framework of viscous strain hardening.

Development of Spring Potentials

The inclusion of point-like slip-links in the model provides a complication in the definition of spring potentials: a slip-link will generally be attached to a spring at some position between two beads, splitting a spring into two "subsprings" containing fractions f and $(1 - f)$ of the spring respectively (f will be treated as a dynamical variable below, to allow for chain motion through the slip-link). The two subsprings will in general not be colinear, so as to allow for independent three-dimensional motion of the two beads (subject to the spring potential), as illustrated in Figure 1. We require spring potentials appropriate for (i) the "one-spring" potential, for a spring connecting two beads together, with no slip-link, and (ii) the "two-spring" potential, for the subsprings created when a slip-link is present between two beads (this spring potential must include the energy for the subspring end-to-end separation, and also a "chemical potential" for variations in f). These two potentials are not independent. For self-consistency, it should be the case that averaging over the position of the slip-link (subject to Boltzmann weighting) for a pair of subsprings should result in an effective potential energy between the beads identical to the potential in the absence of a slip-link altogether (here there

WILEY ONLINE LIBRARY

is an implicit assumption of local equilibrium at length-scales smaller than the beads; we are therefore assuming at least some local chain mobility induced by thermal motion or plastic flow). For the case of linear (Gaussian) spring potentials, the definition of self-consistent potentials obeying this constraint is trivial, but not for nonlinear spring potentials. We have adopted a pragmatic approach, using numerical approximations and potentials related to the FENE spring potential.

Details of the rationale for our spring-potentials are given in Appendix A; here we outline the main features. Our "one-spring" potential is obtained via a saddle-point integration over the position of the slip-link for two subsprings each with a FENE spring potential. For a bead-bead separation of x, this gives a potential of form

$$u_{1-\text{spring}} = -\frac{3}{2}\alpha \ln\left(1 - \frac{x^2}{L^2}\right) + \frac{1}{2}\ln\left(1 + \frac{x^2}{L^2}\right) \quad (1)$$

which we use in the absence of a slip-link. (Note that here, and below, we write our potentials in units of the thermal energy, $k_\text{B}T$.)

The saddle-point integration turns out to be reasonably accurate for values of f close to 0.5. It is, however, not accurate for extreme values of f close to 0 or 1 (there is a short sub-spring for which thermal energies access the spring nonlinearity). In these cases, the integration over the slip-link position is dominated by the weaker and longer of the two subsprings. We thus modify our "two-spring" potential so that it has the form of a FENE spring potential near $f = 0.5$ but approaches the form of the one-spring potential close to $f = 1$.

A final modification concerns the functional dependence of the two-spring potential on f. In order for the probability distribution of the slip-link position, f, along a spring to be uniform, we require the following normalization condition:

$$p(f) = \int_0^\infty 4\pi x_\text{s}^2 \exp\left(-u_{2-\text{spring}}(x_\text{s}, f)\right) dx = 1. \quad (2)$$

where x_s is the bead-sliplink separation. To account for this, we add an extra term, whose form is motivated in part by the observation that a short subspring explores a typical volume scaling as f^3 whilst a longer subspring explores a typical volume scaling as $f^{3/2}$.

Following these modifications, the resulting potential is of form:

$$u_{2-\text{spring}} = -\left(\frac{3}{2}\alpha - 2 + 32\left(f - \frac{1}{2}\right)^4\right) f \ln\left(1 - \frac{x_\text{s}^2}{f^2 L^2}\right)$$
$$+ 8\left(f - \frac{1}{2}\right)^4 \ln\left(1 + \frac{x_\text{s}^2}{L^2}\right) - \ln\left(\frac{a}{f^3} + \frac{b}{f^2} + \frac{c}{f^{3/2}} + df^4\right) \quad (3)$$

where the constants a, b, c, and d are determined numerically by varying the value of f between 0 and 1 and requir-

TABLE 1 Parameters Used in the Simulations

	Symbol	Value
Parameters for spring potential	α	6.434
	L^2	25
	a	0.0026
	b	0.0114
	c	0.026
	d	0.0009
Number of sliplinks per bead	Ψ	1/9
Hop length	h	0.5
Strain induced hops	ε_h	0.02

ing that the normalization condition, eq 2, holds for all f.

These potentials, as given above, are undefined beyond their limit of extensibility. To allow the Monte-Carlo scheme described below to function smoothly, we modify the potentials so that beyond a cut-off (set to within 1% of the limit of extensibility) we use a linear extrapolation of the potentials. In practice, none of the results reported here involve extension of springs beyond their limit of extensibility, but it is likely that trial moves in the Monte-Carlo scheme do take springs beyond the extension limit. Values for all parameters used in the simulation are given in Table 1. The values chosen for L and α are such that, for a single spring in equilibrium, $\langle x^2 \rangle = 3$.

Dynamic Monte Carlo Simulation Scheme

For simulation of chain dynamics we use a dynamic Monte Carlo scheme, based on the principle of detailed balance. As is standard in such schemes, a trial change of state of the system (e.g., a change in a bead position) is generated randomly, and the trial move accepted with a certain probability based on the change of energy. For the hopping of beads, we have in mind the physical picture that, in the glassy state, chain motion is an activated process proceeding via changes of state which involve the traversal of large energy barriers. We suppose that if a chain becomes strongly stretched it can "tilt" the local energy landscape in such a way as to reduce the energy barriers towards moves which reduce the chain stretch, increasing the rate of such moves (and, correspondingly, increase barriers towards moves which increase the chain stretch). To model this, we introduce a novel hop acceptance criterion (described in Appendix B) designed to mimic this physical picture, whilst retaining detailed balance. This acceptance criterion involves a parameter p_0 which is the probability of accepting a trial move with zero change in energy. p_0 is in principle related to the height of the energy barrier ΔE via $p_0 \sim \exp\left(-\Delta E\right)$ and is given a small value in the glassy state (in practice, by "small" we mean less than 0.001; we show that within this regime the actual value chosen makes no difference provided one adjusts the strain rate appropriately). In practice, the advantage of using this acceptance criterion (as opposed to, for example, the Metropolis[30] scheme) with small p_0 is that (i) it allows the algorithm many attempts at possible trial moves, so as to search for

energetically optimal moves (this gives the algorithm the opportunity of running without overstretching bonds), and (ii) it strongly favors moves towards lower energies as compared to moves with neutral energy change (this means that the stresses reported in, for example, Figure 4 below are lower than they would have been if we had just used the Metropolis[30] criterion).

Within one time-step of our algorithm, we make three types of trial Monte Carlo moves: thermally activated bead hops, strain-induced bead hops, and slip-link moves.

Thermally Activated Bead Hops

A bead is chosen at random, and a possible trial change of position is chosen, by changing each of the x, y, and z coordinates by random numbers uniformly distributed between $\pm\sqrt{3}h$ (so that the hop vector has the property $\langle \Delta \mathbf{x}^2 \rangle = 3h^2$). For polymers in the (marginally) glassy state, we consider such motion to be activated, that is, to change its configuration, a bead will typically have to traverse some energy barrier due to the surrounding chains. Thus, we employ our novel acceptance criterion, with probability given in eq B3. The parameter p_0 is given a suitably small value. Since the main feature of this choice of acceptance criterion is the increase (or decrease) of the acceptance probability relative to hops with zero energy change, we can anticipate that our results should converge with decreasing p_0 (i.e., the stress-strain curve becomes independent of p_0) provided (i) one accounts and compensates for the decreased rate of acceptance of hops with zero energy change, and (ii) the majority of hops have energy change in the range $|\Delta u_{12}| < 2 \ln p_0$ (see Appendix B).

Strain-Induced Bead Hops

We wish to include in our algorithm the (likely) possibility that motion of the chains can be induced by flow of the material. We model this in as simple manner as possible by including an extra set of hop attempts at a rate proportional to the rate of strain (each bead, on average, makes such a hop every ε_h strain units). In an identical manner to thermally activated hops, a bead is chosen at random, and a possible trial change of position is chosen. However, we envisage that such hops are not activated (in the sense of traversing large energy barriers) but that, rather, during flow the opportunity for a bead to change position will regularly open up as the surrounding chains are also moved; given such an opportunity, the chain must either hold its position or move to the new state (and the chain chooses between these two options according to their equilibrium Boltzmann probabilities). Thus, a natural acceptance probability is the one given in eq B2.

Slip-Link Moves

As described earlier we use point-like slip-links to model the fact that the polymer chains are entangled with each other and this restricts their motion. In addition to bead motion, we need to model the motion of the chain through each slip-link. For each slip-link, the variable f represents the fraction of the spring on each side of the sliplink. In a trial move, we choose a slip-link at random, and a random change in f

(between $+/-1$). Several possibilities could occur (note that, in none of these do the bead positions or the slip-link position change, only the value of f). In each case, we use the Metropolis[30] criterion (B1) to determine acceptance (or not) of the trial move.

  i. The change in f could result in the slip-link remaining on the same spring. Acceptance of the move is based on the change in energy for that spring alone.
 ii. The change in f could take the slip-link beyond the end of the spring, in which case the trial move becomes a move to an adjacent spring. If the adjacent spring is occupied already by another slip-link, the move is rejected (we allow no more than one slip-link per spring). Otherwise, acceptance of the move is based on the change in energy for both springs involved.
iii. A special case of (ii) above occurs where the current spring is the end spring in the chain and the change in f takes the slip-link beyond the end of the spring. In this case the trial move becomes removal of the slip-link (i.e., equivalent to the chain end passing through the slip-link). This is accepted with probability $1 - \psi$, where ψ is the equilibrium fraction of springs on which a slip-link is present (i.e., $\psi = N_e^{-1}$ where N_e is the number of beads per entanglement). This factor $1 - \psi$ accounts for the contribution to the effective chemical potential of sliplinks arising from the constraint that only one sliplink per spring is permitted in the simulation.

Since sliplinks can move off the ends of chains, it is necessary to include the reverse process of addition of sliplinks to chain ends, so as to maintain the equilibrium statistics. To do this, chain ends are sampled at the same rate as sliplinks. If the terminal spring at a chain end is unoccupied by a sliplink, then a random number f is chosen, to represent the distance in from the end that a new sliplink will be placed. This new sliplink is then accepted with probability $\psi(1 - f)/2$ (reflecting the probability of the reverse move: that a sliplink is found on this spring, at position f, and is removed from the chain by a random sliplink move). The position of the added sliplink is chosen randomly, based on the position of the two beads attached to the spring and Boltzmann statistics.

In a single simulation "step," we choose N beads at random (where N is the total number of beads) and perform a thermally induced hop attempt on each such bead (this is in contrast to a common method used for simulating a "Rouse" chain in which all beads simultaneously take a small random hop (as, for example, in ref. 29); because our trial moves involve large steps we have to execute them one bead at a time, and to choose beads randomly as opposed to sequentially). Secondly, we generate a random number, according to Poisson statistics, representing the number of strain induced hop attempts in the system during one simulation step. The mean of this Poisson distribution is $N\Delta\varepsilon/\varepsilon_h$ where $\Delta\varepsilon$ is the increment in Henky strain during one simulation step, and ε_h is an adjustable parameter which is the typical strain for a local plastic rearrangement. Having generated this random

number, we choose that number of beads at random and make strain-induced hop attempts for them as described earlier. Thus, each bead will, on average, make one strain-induced hop attempt within a deformation of Henky strain ε_h. Finally, we choose $5N_s$ slip-links at random and perform the attempts at sliplink moves on each chosen slip-link as described earlier. The factor 5 has been chosen via trial and error so that the terminal relaxation time (by reptation) of the system becomes independent of the number of random sliplink moves for all p_0 values (i.e., in this limit, bead friction dominates over sliplink friction).

The above simulation step, so defined, guarantees that after repeated steps the system will (eventually) reach an equilibrium distribution consistent with the spring free energy and average slip-link number. Deformation can be applied to the system during a step by affine convection of slip-links and beads. We additionally note that, following a large strain, the process of chain retraction[24,25] occurs and (as is well known in sliplink simulations[27,28]) the number of sliplinks decreases. There is no consensus as to what is the correct thing to do when this occurs. We have investigated two possible assumptions among many, (i) allowing the sliplink number to decrease without other intervention, and (ii) making an attempt to keep the number of sliplinks constant. Since the number of sliplinks fluctuates even at equilibrium, it is not possible to do this exactly. We have taken a pragmatic approach, and introduced sliplinks at random positions along chains when the number of sliplinks falls below three standard deviations from the average (such events are very rare under normal equilibrium fluctuation, but occur quite readily during chain retraction). In all results reported in this article, we use the second option (i.e., keeping number of sliplinks roughly constant), though qualitatively similar results are obtained using either assumption.

This basic simulation step allows us to perform a number of different simulation procedures which we describe in the following section.

SIMULATION PROCEDURES

Calculation of Monomer Diffusion Constant

For calculating the important time scale of the chains such as, τ_e (entanglement time), τ_R (Rouse time), τ_d (reptation time) in the unit of number of simulation steps, it is important to calculate the effective monomer diffusion constant (D_{mon}). We perform equilibrium simulations on long chains in the absence of sliplinks and measure $\langle (R_n(t) - R_n(0))^2 \rangle$, the mean square displacement of a bead with the index n from time $t = 0$ to a certain time t. According to the Rouse model, at timescales much longer than the monomer relaxation time, but shorter than the chain Rouse relaxation time, this quantity should scale as[24]

$$\frac{\langle (R_n(t) - R_n(0))^2 \rangle}{t^{1/2}} = 2\sqrt{\frac{3D_{mon}b^2}{\pi}} \qquad (4)$$

thus allowing D_{mon} to be extracted from the simulation data.
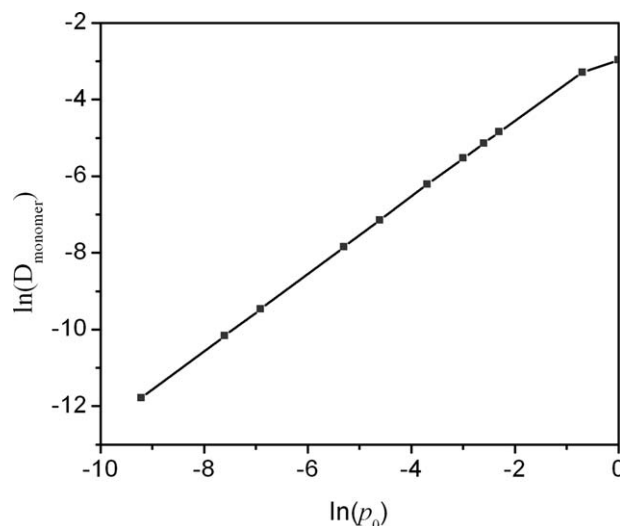
FIGURE 2 Variation of monomer diffusion constant (D_{mon}) with hop probability (p_0).

Using simulation parameters given in Table 1 we varied the hop probability, p_0 from 1 to 0.0001. Figure 2 shows the calculated D_{mon} with variation of p_0 in logarithmic scale. D_{mon} increases monotonically with p_0, and we note that, at small values of p_0, D_{mon} is directly proportional to p_0, allowing D_{mon} to be extrapolated beyond the range of p_0 we have simulated (for $p_0 < 0.1$ a good approximation is $D_{mon} = 0.078\ p_0$, but note that all points shown in Figure 2 are simulation results, not extrapolations).

Using the monomer diffusion constant of the polymer chain, we can calculate the Rouse time and estimate the entanglement time for different sizes of the polymer chain. In all simulations we performed, the average number of beads per sliplink was set to a value of 9 (i.e., $\psi = 1/9$, $N_e = 9$) and so we estimate the entanglement time as the Rouse time of a chain with 9 beads.

Table 2 shows these time scales for $p_0 = 1$, 0.5 and 0.1 (values for smaller p_0 may be extrapolated from the $p_0 = 0.1$ results) and $N = 72$, 90 and 125 beads. Knowledge of these timescales is essential if we are to match the times for annealing and stretching in the experiments of Hine et al.[26] in the units of simulation time step.

Uniaxial Deformation and Annealing

The experiments we wish to address with our model involve an initial uniaxial stretch, followed by annealing of the sample at constant length for various time intervals. The birefringence of annealed samples was measured. Some annealed samples were subjected to a shrinkage test (described in the next section) whilst others were subjected to further stress-strain tests, typically at a lower temperature just within the glassy regime. We aim to match the experimental procedures as closely as possible within our simulations.

We simulate the initial stretch (usually by a factor of 4) by uniaxial deformation at constant rate within 666 simulation time steps, using a value of $p_0 = 0.5$. With these parameters,

TABLE 2 Monomer Diffusion Constant and Characteristic Relaxation Timescales (in Units of Simulation Steps) for Three Values of p_0 and Three Different Chain Lengths of 72, 90, and 125 Beads

	Monomer Diffusion Const.	Entanglement Time	Rouse Times			Approx. Reptation Time		
P_0	D_{mon}	τ_e	τ_R (72)	τ_R (90)	τ_R (125)	τ_d (72)	τ_d (90)	τ_d (125)
1.0	0.0511	160	1.03×10^4	1.60×10^4	3.09×10^4	2.46×10^5	4.80×10^5	1.28×10^6
0.5	0.0370	222	1.42×10^4	2.22×10^4	4.27×10^4	3.40×10^5	6.64×10^5	1.78×10^6
0.1	0.0078	1041	6.66×10^4	1.04×10^5	2.01×10^5	1.59×10^5	3.12×10^6	8.36×10^6

we match closely the experimental deformation time, which is of order $3\tau_e$. Constant volume is imposed during the deformation, by contracting the simulation perpendicular to the stretch direction.

We anneal by repeated simulation steps, maintaining $p_0 = 0.5$, and save the simulation state at various predetermined times for subsequent simulations.

In the experiments, further stretching was applied at a rate of $\dot{\varepsilon} = 0.00833$ s^{-1} and at a temperature of 105°C, which we take to be in the marginally glassy state (there was an observed yield stress). Nevertheless, this temperature is still sufficiently high for time temperature superposition to be extrapolated so as to obtain the effective entanglement relaxation time at this temperature, giving $\tau_e = 6870$s. Thus, for the experiments, $\dot{\varepsilon}\tau_e \approx 57$—it is this quantity which we attempt to match in the simulations. We anticipate that thermal motion of the beads will be an activated process, occurring via traversing energy barriers, so it is appropriate to use a small value of p_0 in the simulations. Since the simulation τ_e is a function of p_0, the appropriate extension rate (measured as strain per simulation step) must also vary with p_0 (so as to match $\dot{\varepsilon}\tau_e \approx 57$). Suitable rates, for different values of p_0 typically used are shown in Table 3. We note that, assuming Rouse scaling of relaxation times, $\dot{\varepsilon}\tau_e \approx 57$ corresponds to a strain rate, normalized by an equilibrium bead relaxation time of $\dot{\varepsilon}\tau_{bead} \approx 0.7$. Although this means the extension rate is close to the limit of applicability of our level of coarse-graining, we note that out of equilibrium, and given our novel hop acceptance criterion, strongly stretched chains increase the rate of relaxation towards lower energy states, so the effective bead relaxation time is, in practice, reduced.

The spring potentials (1) and (3) allow us to calculate the forces acting within the chain at each step. The average stress per bead along the applied force direction can be calculated by using following expression.

$$\left\langle \sigma_{xx} - \frac{1}{2}\left(\sigma_{yy} + \sigma_{zz}\right)\right\rangle_{bead} = \frac{1}{n}\sum_{i=1}^{n}\left(f_x x - \frac{1}{2}\left(f_y y + f_z z\right)\right)_i \quad (5)$$

Where n is the total number of segments present in the system. x, y, and z are the components of the segment vector and f_x, f_y, and f_z are the components of the force in spring i. In using this expression for the stress, we explicitly include

only intramolecular forces (i.e., we are not directly accounting for viscous contributions to the hardening stress; we are assuming that the stress contributions from individual chains may simply be added, for which there is some support from simulation of binary blends[15]).

We also calculate the segment orientation function (which we take to be a measure of birefringence) during annealing as follows:

$$\text{Segment orientation} = \frac{1}{n}\sum_{i=1}^{n}\left(x^2 - \frac{1}{2}\left(y^2 + z^2\right)\right)_i \quad (6)$$

If each of our springs were representing a subchain from an idealized freely-rotating bond model, then within the linear regime the potential this segment orientation functions is directly proportional to the orientation function $P_2(\cos\theta)$ of the freely rotating bonds.

Shrinkage Measurement

During a shrinkage experiment, the sample is placed in a hot oil bath, and shrinkage occurs at a rate determined by a balance between elastic chain stresses and internal viscosity of the sample. We mimic this in the simulations. At each time step, we calculate the stress due to the chains. We then assume an additional sample viscosity, μ, obtaining a shrinkage rate of

$$\dot{\varepsilon} = -\frac{1}{\mu}\langle\sigma_{xx} - \frac{1}{2}(\sigma_{yy} + \sigma_{zz})\rangle_{bead} \quad (7)$$

from which we obtain the shrinkage strain for the current time step. After a repeating this procedure over a long period (of order the reptation time of the chains) the simulated systems fluctuate about a fixed length (due to small fluctuations in stress) and the shrinkage is measured as

$$\text{Shrinkage} = \frac{\text{Original length}}{\text{Final length}} \quad (8)$$

TABLE 3 Appropriate Deformation Rates (in Simulation Units) so as to Match $\dot{\varepsilon}\tau_e \approx 57$ for Three Values of p_0

	$p_0 = 0.001$	$p_0 = 0.0005$	$p_0 = 0.0001$
$\dot{\varepsilon}$ (strain per step)	5.37×10^{-4}	2.68×10^{-4}	5.28×10^{-5}

In the absence of molecular motion, the balance between viscosity μ and bond elasticity provides a shrinkage relaxation time of order μ timesteps. With molecular motion, and provided μ is smaller than the typical molecular relaxation timescales, the shrinkage dynamics are actually dominated by a competition between fast internal modes of the chains (which contribute an effective viscosity of their own) and long-lived elastic modes due to entanglements. Thus the shrinkage is independent of μ in this regime. We use a value of $\mu = 100$ and $p_0 = 0.5$, measuring the sample shrinkage as a function of annealing time following a step strain. A few simulations using $\mu = 500$ revealed no significant difference to the results.

RESULTS AND COMPARISON WITH EXPERIMENTS

In this section we describe the results of a set of simulations designed to mimic the experimental procedure of Hine et al., and demonstrate that our simulations match, at a qualitative level, all the observations made in those experiments. Simulations were performed for monodisperse chains (with 72, 90 and 125 beads per chain, 500 chains in total) and also for a polydisperse (PDS) set of chains in which the distribution of chain lengths was chosen so as to mimic the molecular weight distribution of the sample used by Hine et al.[26] (PDI=2.7, weight-average number of beads = 137). In all simulations, the average number of beads per sliplink, N_e, was set to a value of 9 (i.e., $\psi = 1/9$).

We make comparison with experimental data published by Hine et al.[26] on the polydisperse sample together with new data from a monodisperse sample (260k polystyrene[22,23]) subjected to exactly the same experimental protocol as detailed in Hine et al. For the purposes of comparison, we assume each simulation bead is roughly equivalent to a unit of PS with mass 2k atomic mass units (corresponding to around 18 chemical monomers, which we assume is sufficiently large to allow a coarse-grained model with no chemical detail; so, there are roughly 8-9 beads per entanglement). Thus the 125 bead simulations are appropriate for qualitative comparison with the data from the monodisperse sample.

Bond Orientation and Shrinkage Following Stretch and Annealing

Following the procedure detailed in section 3.2, a set of simulations was performed in which the model was stretched by a factor of 4, and annealed for a range of times at fixed length. For each annealing time, we measure the local bond orientation using eq 6, and the sample shrinkage as detailed in section 3.3.

Figure 3 shows the measurement of bond orientation and shrinkage of chains of different bead size (72, 90, 125 and polydisperse (PDS)), as a function of annealing time. The important relaxation time scales τ_e and τ_R for the monodisperse samples are indicated in the figure. These results are in excellent qualitative agreement with the experiments, which are also shown in Figure 3, both for the polydisperse and monodisperse samples. It was found to be impossible to

anneal the stretched monodisperse samples beyond 45 minutes at 115 °C without sample rupture (which is most likely an instability due to relaxation of chain stretch, as exemplified in ref. 31).

The bond orientation (which we take to be correlated with the experimental birefringence) begins to fall almost immediately upon annealing. The majority of the bond orientation is relaxed at times significantly earlier than the chain Rouse time τ_R (although there is clearly a wide distribution of relaxation times—bond orientation, and stress, is not fully relaxed before annealing times of order the chain reptation time).

In contrast, in all the simulations the shrinkage barely changes for annealing times less than about $3\tau_e$ (666 simulation time steps: here τ_e is 222 simulation time steps). Figure 3 illustrates particularly well how the characteristic annealing time for loss in sample shrinkage changes with the chain length: it appears to shift in much the same way as the chain Rouse time (whilst again exhibiting a broad distribution of relaxation times).

These same observations in the experiments were used to infer that the initial stretch produced significant orientation at the bond lengthscale, much of which could be relaxed by sub-tube-diameter motion of the chains. This explained the rapid initial drop in sample birefringence upon annealing. The sample shrinkage, however, is evidently not affected by these initial bond-lengthscale relaxations, and it was suggested by Hine et al.[26] that the shrinkage was related to structure at the entanglement lengthscale. The present simulations appear to support this interpretation.

Figure 3 also indicates that reducing the chain length results in a drop in the initial values of both birefringence and shrinkage. This is a result of the finite time for the initial stretch (666 simulation time steps—ca. $3\tau_e$). Some chain relaxation is taking place during this initial stretch and the effects are more prominent for shorter chain lengths. A timescale of $3\tau_e$ is sufficient to relax perhaps the outermost two entanglement segments of a chain, and this represents a significant fraction of the shorter chains in this study. The polydisperse sample contains a range of size of the chains and the rapid relaxation of the smaller chains during the initial stretch appears to have a substantial effect. We note also that, immediately following the initial stretch and for short annealing times, the experimental birefringence for the monodisperse sample is significantly higher than that of the polydisperse sample. This feature is matched well by the simulations: the average bond orientation for the 125 bead simulations is significantly higher than that of the polydisperse sample. This is due to the presence of short chains in the polydiperse sample, which are not strongly deformed in the initial stretch and which relax any orientation quickly following that stretch.

Stress-Strain Behavior Upon Further Stretching

Further stretching of the annealed models was carried out as described in section 3.2, and the stress (eq 8) recorded as
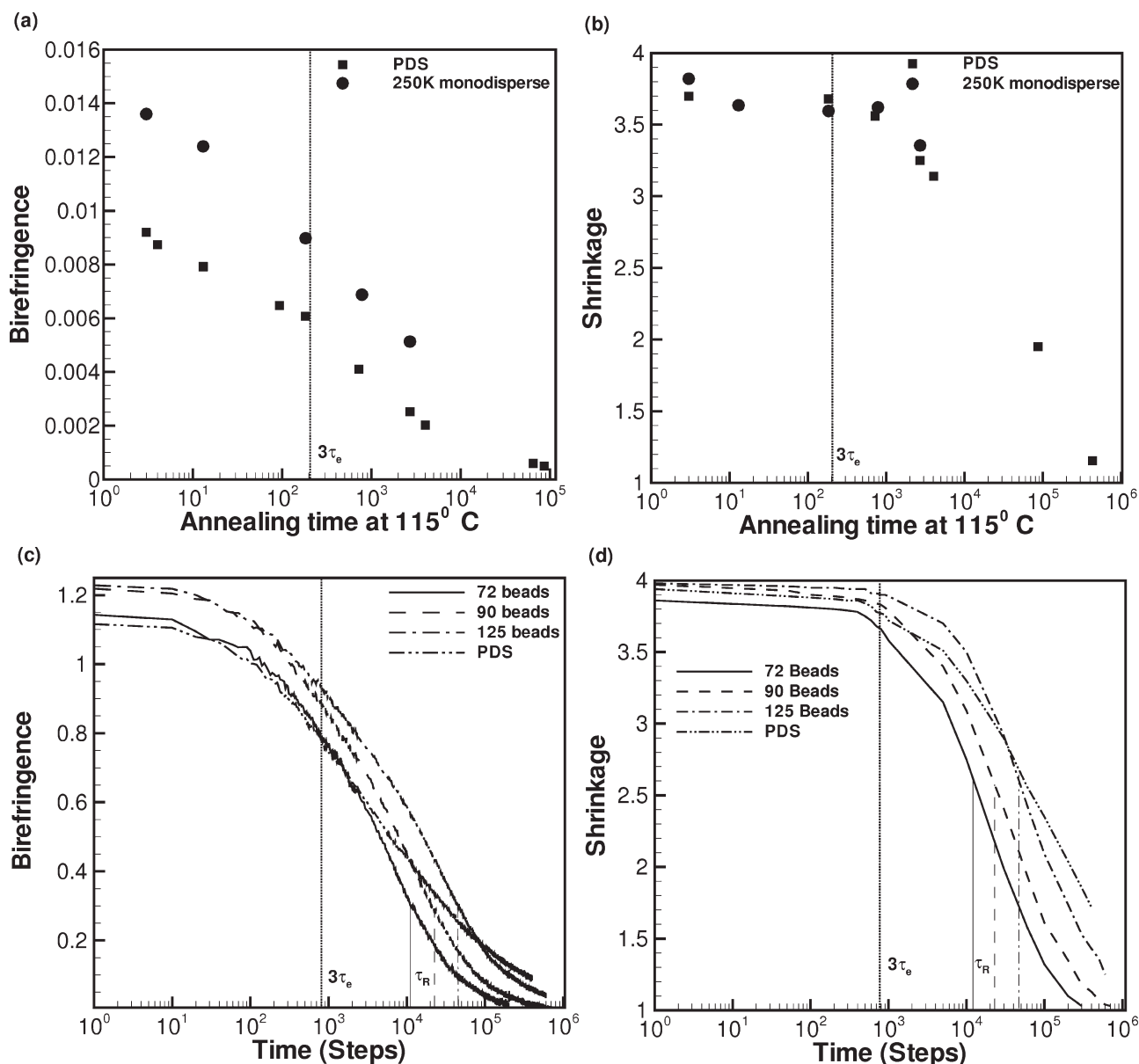
FIGURE 3 (a and b) Birefringence and thermal shrinkage of experimental drawn and annealed samples versus annealing time, for both polydisperse (PDS) and monodisperse material (c and d) equivalent results for simulations of polydisperse (PDS) polymers and monodisperse polymers of varying length.

a function of strain. We used a range of (small) values of p_0 for this, whilst also varying the extension rate such that $\dot{\varepsilon}\tau_e \approx 57$. With this constraint, we found that the results were independent of p_0 within the range 10^{-2} to 10^{-4}.

Figure 4 shows the true stress-true strain curves of the 125-bead and PDS simulations following annealing for a range of times, together with the equivalent results for the experimental samples. We emphasize that the stress reported for the simulations is the intrachain stress only, arising from the spring potentials—this is intended to represent the strain-hardening contributions to the stress. We have not attempted to model the additional contributions to stress arising from yield and glassy flow. As a result our model

does not exhibit the very obvious yield stress and initial plateau exhibited in the experiments. This issue will be discussed further in the conclusions. In agreement with the experiments of Hine et al.,[26] the results show that, with increasing annealing time, there is fall in the hardening stress, and that this fall begins to occur even with very short annealing times (significantly less than 666 simulation time steps).

Hine et al. also made attempts to superpose their stress-strain curves by shifting them along the strain axis. They found that, for short annealing times (within the range where the sample shrinkage was unaffected by annealing) practically perfect superposition over the whole range of
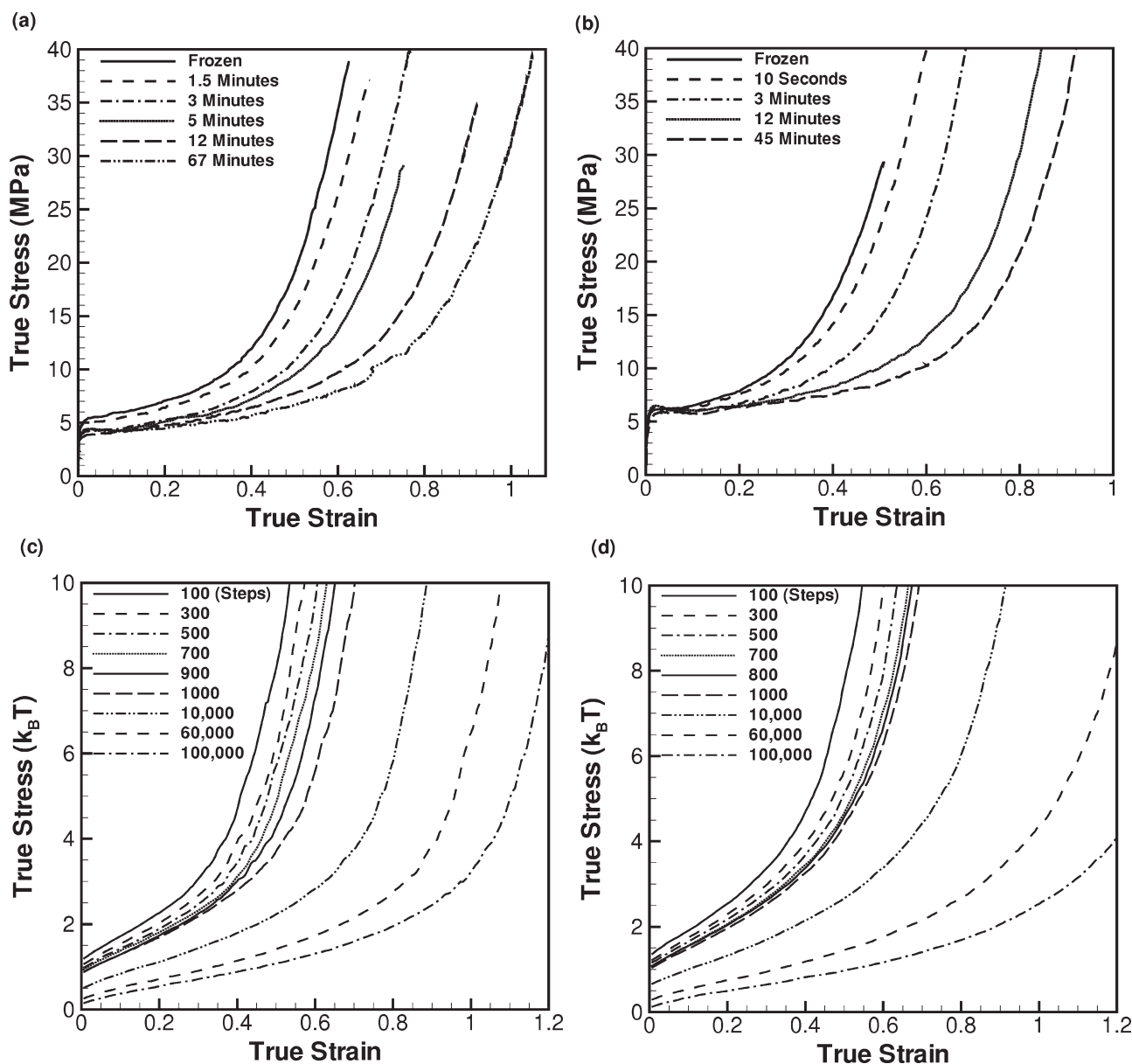
FIGURE 4 Stress-strain curves for (a) experimental polydisperse, (b) experimental monodisperse, (c) simulated polydisperse, and (d) simulated 125-bead monodisperse samples, for deformation following deformation by an extension ratio of 4 and annealing over a range of times. Experiments are performed at 105 °C and $\dot{\varepsilon} = 0.00833$ s^{-1} following annealing at 115 °C.

strain could be achieved via such a shift, but that for longer annealing times this was no longer possible. Hine et al. chose to superpose all the curves in the low-stress region (termed the "weak strain hardening region") but then found that the curves no longer superposed in the higher stress region (termed the "strong strain hardening region").

In Figure 5 we attempt to mimic the superposition procedure of Hine et al. by shifting the curves along the strain axis so that they pass through the same point at a particular value of stress (we have chosen this value to be $1k_{B}T$ per bead so as to attain superposition in the weak strain hardening region). We also perform the same procedure on the experimental data, aiming for superposition at a stress level of

7 MPa. In the simulation data, it can be seen that, the superimposition of the curves are very good for less annealed samples (annealed for 100–700 steps), but the higher annealed samples, particularly 1000 steps onwards the superposition is less successful. As with the experiments, good superposition is possible for the range of annealing times for which the sample shrinkage remains unaffected.

The experimental results of Hine et al. suggested that superposition in the weak strain hardening region was always possible for all annealing times (even if not for the full stress-strain curve). The simulation results of Figure 5 suggest that this is approximately, but not exactly true: there is some fanning out of the curves even in the weak strain
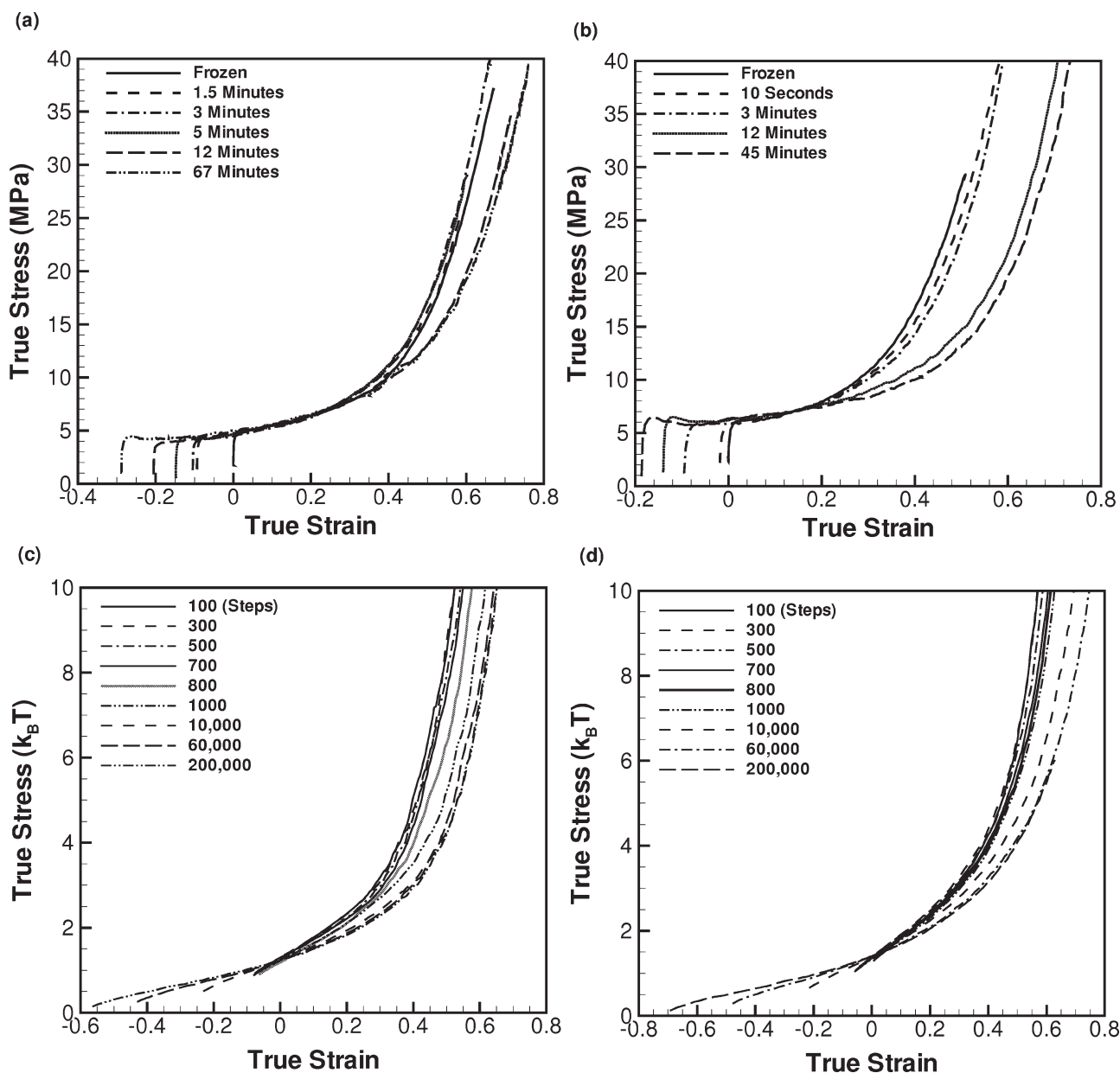
FIGURE 5 Data from Figure 4, shifted along the true strain axis so as to achieve superposition at 7 MPa [experimental (a) polydisperse; (b) monodisperse) or $1k_BT$ per bead (simulation (c) polydisperse; (d) monodisperse].

hardening region for the longer annealing times – this effect appears stronger for the 125 bead simulation than for the polydisperse case. In fact, close inspection of the shifted experimental data (also shown in Fig. 5) indicates this effect is weakly present there also, perhaps most obviously so for the monodisperse data. For the polydisperse case, the effect is sufficiently weak so as to be largely masked by the experimental error.

Superposition of Stress-Strain Curves for Samples with Different Initial Draw Ratio

The aforementioned observations led Hine et al. to speculate that the shape of the strain hardening curve (i.e., with respect to superposition by shifting along the true strain axis) could be correlated with sample shrinkage. To test this,

Hine et al. also performed a comparison of stress strain curves for two polydisperse samples: one drawn by a factor of 3 but then not annealed (so that its shrinkage—the factor by which it contracts upon heating in an oil bath above the glass transition temperature—was measured to be 3), and a second drawn by a factor of 4 but annealed until its shrinkage was 3. Hine et al. found that the stress-strain curves of these two samples could be perfectly superposed with a shift along the strain axis (such an experiment was not possible for the monodisperse samples, because the samples always ruptured before their shrinkage fell to 3).

Figure 6 demonstrates exactly the same phenomenon within the simulations, for the polydisperse model (in the simulations, exactly the same result is observed for the

WILEY ONLINE LIBRARY

(a)

(b)
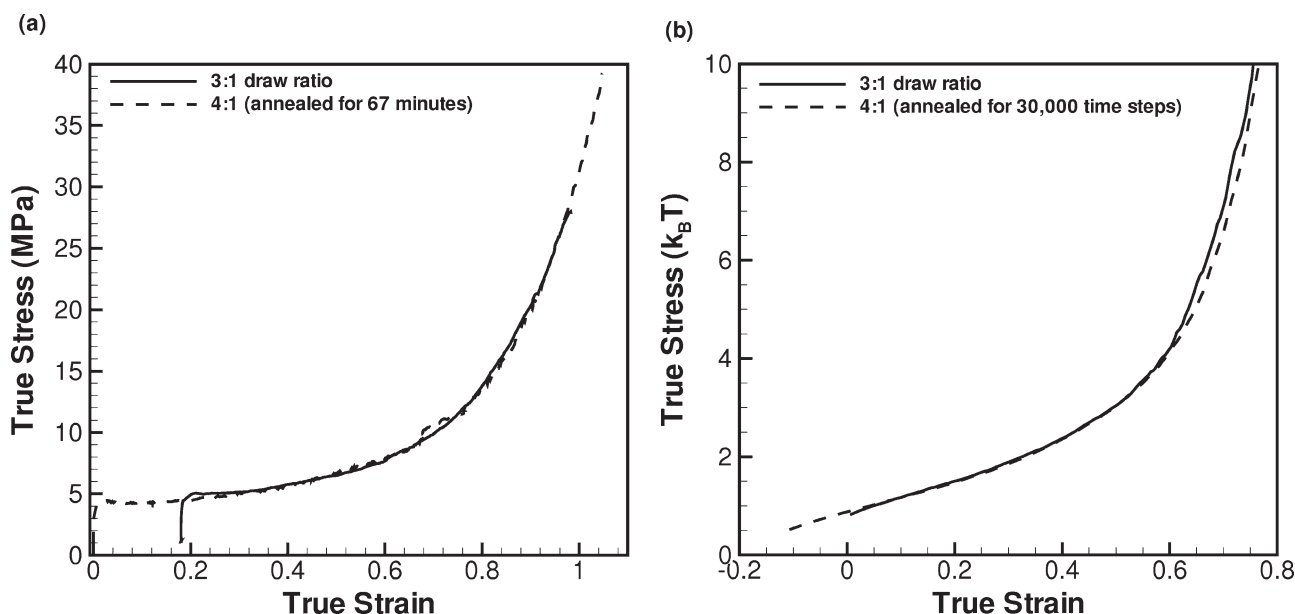
FIGURE 6 A comparison of true stress-true strain curves for the polydisperse (a) experimental, and (b) simulation samples drawn to 3:1 and frozen immediately and a sample drawn to 4:1 and annealed for (a) 67 minutes, or (b) 30,000 steps (so that the shrinkage in each case ~3). Curves are shifted along the true strain axis so as to achieve superposition.

monodisperse sample). One sample is drawn by a factor of 3 but not annealed and a second drawn by a factor 4 and annealed for 30,000 simulation time steps so that shrinkage of this sample is 2.95. Superposition of the subsequent stress-strain curves of these two samples appears to be practically exact after shifting along the true strain axis. The qualitative explanation offered by Hine et al.[26] for this phenomenon is that both shrinkage, and the shape of the strain hardening curves, are related to entanglement structure. It is thus plausible that samples with the same shrinkage would have similar entanglement structure and so offer similar shapes of strain hardening curve, allowing this superposition. The fact that these qualitative concepts lead to such good superposition in practice nevertheless remains surprising.

### Discussion of Stress-Strain Curves

Hine et al. drew two main conclusions from their data. Firstly, the fact that the stress-strain curves were affected at all by the shortest annealing times (for which birefringence, but not shrinkage, changed) indicated that the initial strain hardening arose from deformation of units smaller than entanglement segments. On the other hand, the shape of the strain-hardening curve (and in particular the transition from weak to strong strain-hardening) seemed to correlate with sample shrinkage, such that samples with the same shrinkage could be superposed. This suggested that the strong strain-hardening region, like the sample shrinkage, may be affected by the entanglement structure, and might involve chains pulling tight between entanglements. Since our simulations appear to reproduce qualitatively the experimental observations, we can hope to be able to test whether the inferences draw by Hine et al. provide an accurate description of the behavior in our simulations.

MICROSCOPIC PROBES OF THE SIMULATION

In this section we present three different projections of our simulation data. Given the large amount of data available, there are many possible such projections, but each of these provides some insight into the typical microscopic behavior.

Firstly, in Figure 7, we show the probability distributions of bond lengths (normalized by the maximum extensibility). These distributions are taken at different values of stress along the stress-strain curves ($2k_BT$, $4k_BT$, $6k_BT$, $9k_BT$), for simulations with different annealing times (100, 1,000, 10,000 time steps), all for the 125-bead monodisperse sample. The stress levels were chosen so that the smaller values are in the weak strain hardening region, where approximate superposition was always possible, whilst the high values were in the strong strain-hardening region, where superposition breaks down. The simulations with annealing for 100 and 1000 steps would nearly superpose for the full range of stress, whilst the simulation with 10000 steps would not superpose in the strong hardening region. It is interesting to note that simulations with the same level of stress show very similar distributions of their bond lengths, at least within this limited set of data. This is despite the fact that the total strain required to produce that stress is different in each case. We also observe that the distribution evolves as the stress level is increased. Although in all cases the majority of bonds are not very strongly stretched, as one approaches the higher levels of stress there are a minority of bonds which approach the maximum extension. At the highest stress level probed here, a small secondary peak appears in the probability distribution at the maximum extension (in fact, for yet higher stresses, the simulation typically exceeds its range of validity, as bonds get taken beyond their
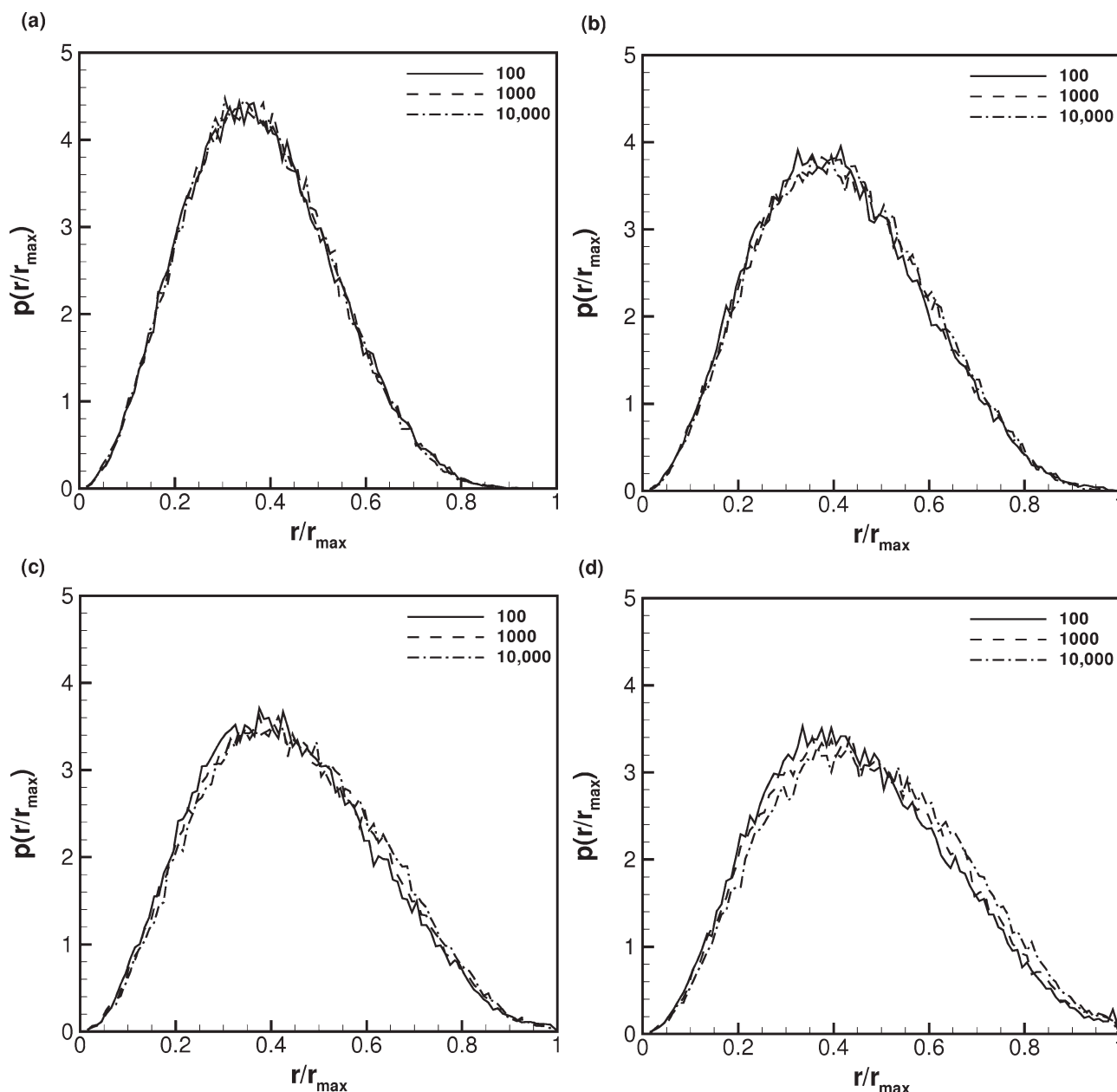
FIGURE 7 Probability distributions of bond lengths (normalized by maximum extension) for models with annealing times of 100, 1000, and 10,000 steps and subsequently stretched to stress levels per bond of (a) $2k_BT$, (b) $4k_BT$, (c) $6k_BT$, (d) $9k_BT$.

"maximum" extension because the dynamic Monte Carlo scheme is no longer able to find suitable hops which keep the bond lengths below this). There are indications, then, that bonds are being pulled tight at the higher levels of stress. These bonds (of course) provide a disproportionate contribution to the stress: for example, once the simulation with 1000 time-step annealing is deformed to give a stress of $9k_BT$ per bond, the 1.3% of bonds with $r/r_{max} > 0.9$ provide 30% of the total stress.

Given that bonds appear to be being pulled tight, the question arises as to whether this is primarily due to the effect of entanglements. Figure 8 shows scatter plots, in which

each point represents a single bond in the simulation. The y-axis position is the ratio of the bond length to its maximum length. The x-axis position is determined from the two sliplinks the bond lies between—it is their separation divided by their maximum separation (based on the amount of chain between them). Plots are shown for the 125-bead simulation, annealed for 1000 time steps, and then subsequently stretched to stress levels of ($2k_BT$, $4k_BT$, $6k_BT$, $9k_BT$). One can clearly see in these plots that, as the stress increases from the weak hardening region (stress $2k_BT$, $4k_BT$) to the stronger hardening region (stress $9k_BT$), that both bonds and pairs of sliplinks are pulled tight, and that there is a strong correlation between these. Although there are some strongly
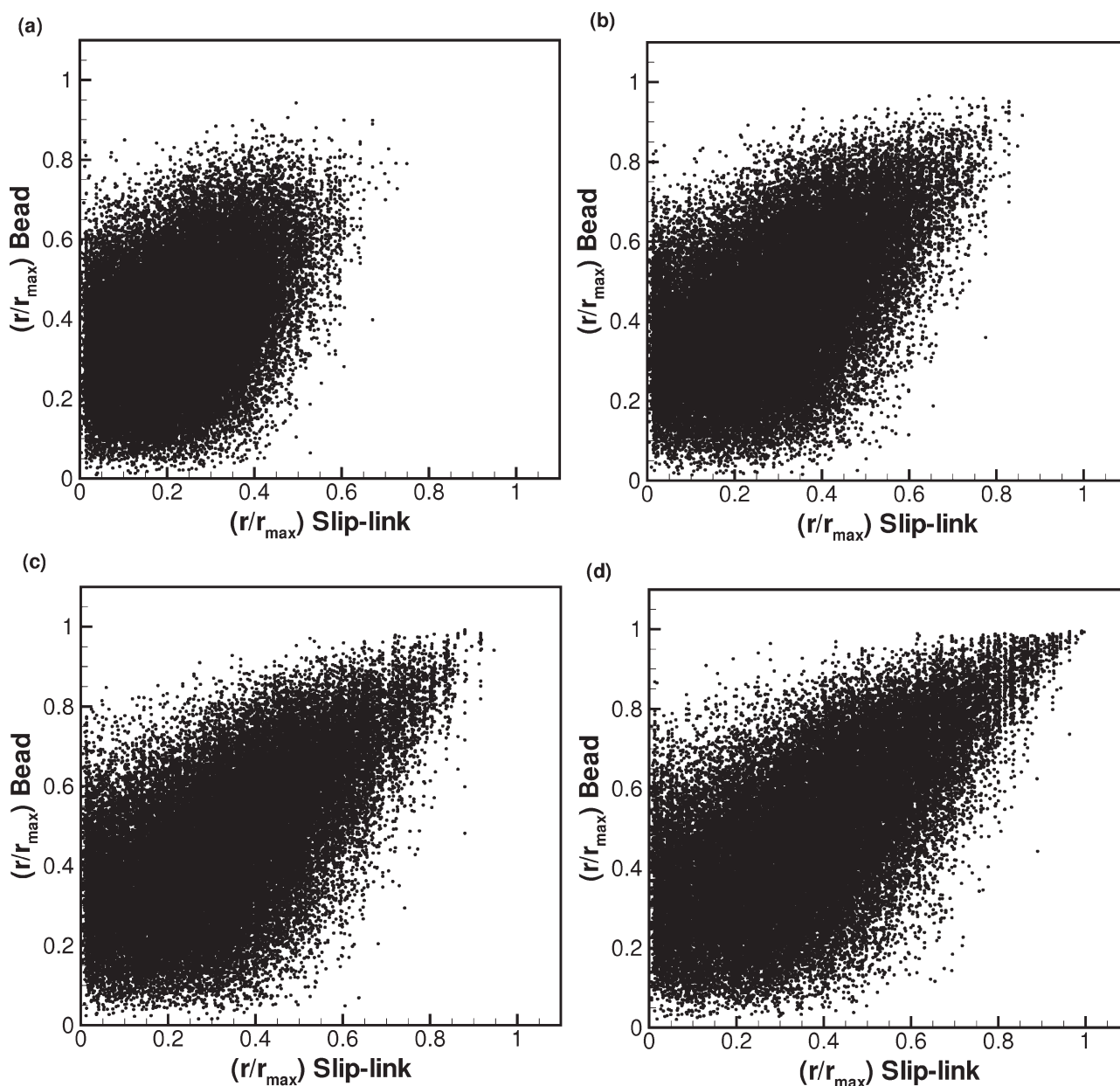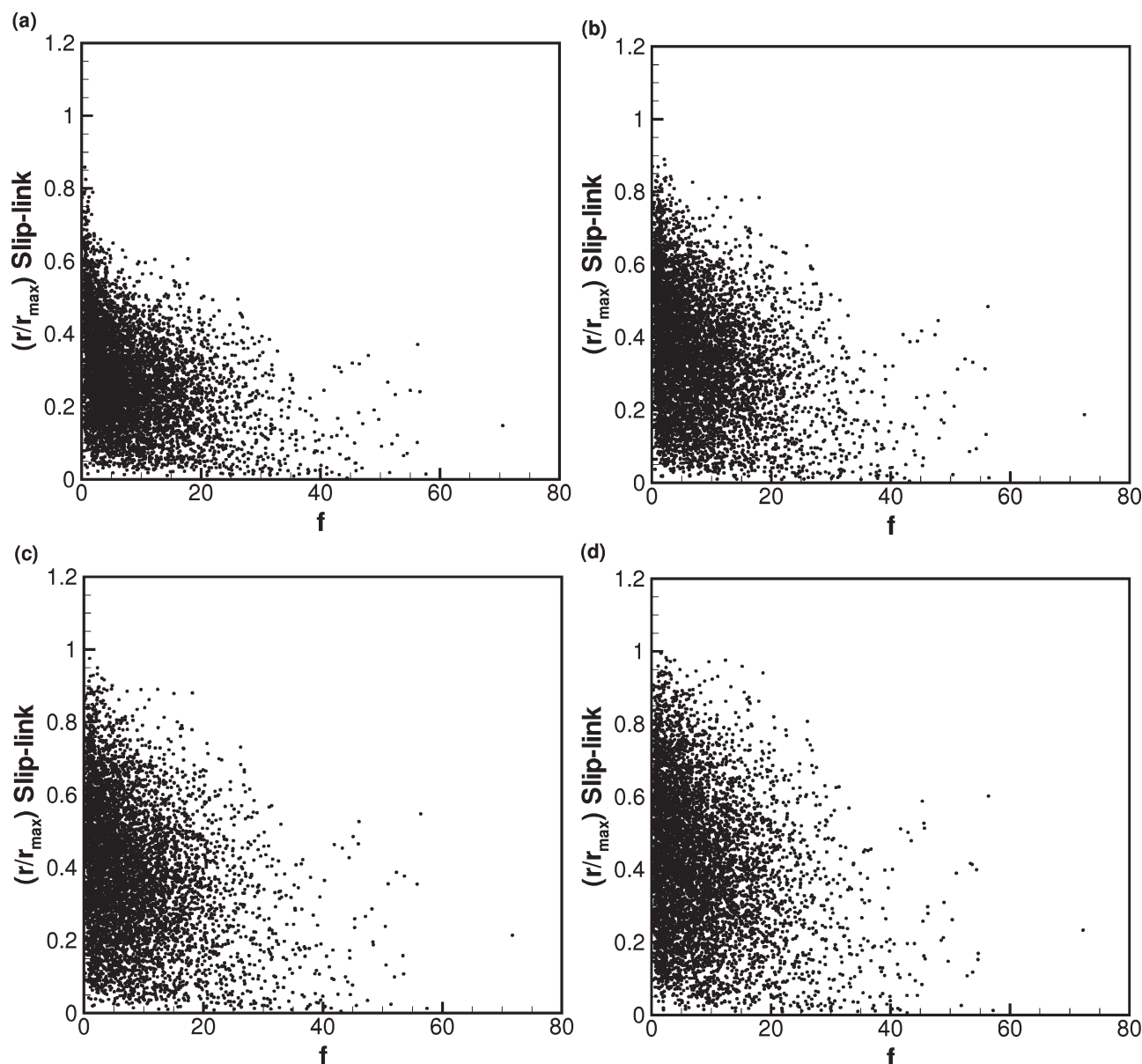
FIGURE 8 Scatter plots for the 125-bead simulation, annealed for 1000 time steps, and then subsequently stretched to stress levels per bond of (a) $2k_BT$, (b) $4k_BT$, (c) $6k_BT$, (d) $9k_BT$: each point represents a single bond in the simulation. The y-axis position is the ratio of the bond length to its maximum length. The x-axis position is determined from the two sliplinks the bond lies between—it is their separation divided by their maximum separation.

stretched bonds that are not held between strongly-stretched entanglement pairs, the majority are. It seems that there are a few rare pairs of entanglements with chain pulled tight between them, and that these are the prime (but not only) cause of strong bond-stretching. The other cause of bond stretching is simply that the internal chain dynamics are slow, so that even in the absence of entanglements some chain stretching occurs (as is observed, for example, in dilute polymer solutions).

A further question that arises is, given there is a distribution of chain lengths between sliplinks in the simulation, whether

there is any correlation between the length of chain between sliplinks and the chain being pulled tight between them. In Figure 9, we show a second set of scatter plots in which each point represents a pair of sliplinks. The x-axis position is the length of chain between those two sliplinks, and the y-axis is their separation, divided by their maximum separation. This plot illustrates that it is of course true that those sliplink pairs with only a short piece of chain between them have a broader distribution of separations when this is scaled by their maximum separation. This is natural, and would be expected even with ideal Gaussian chain statistics (linear springs). So, when deformation occurs, those sliplink
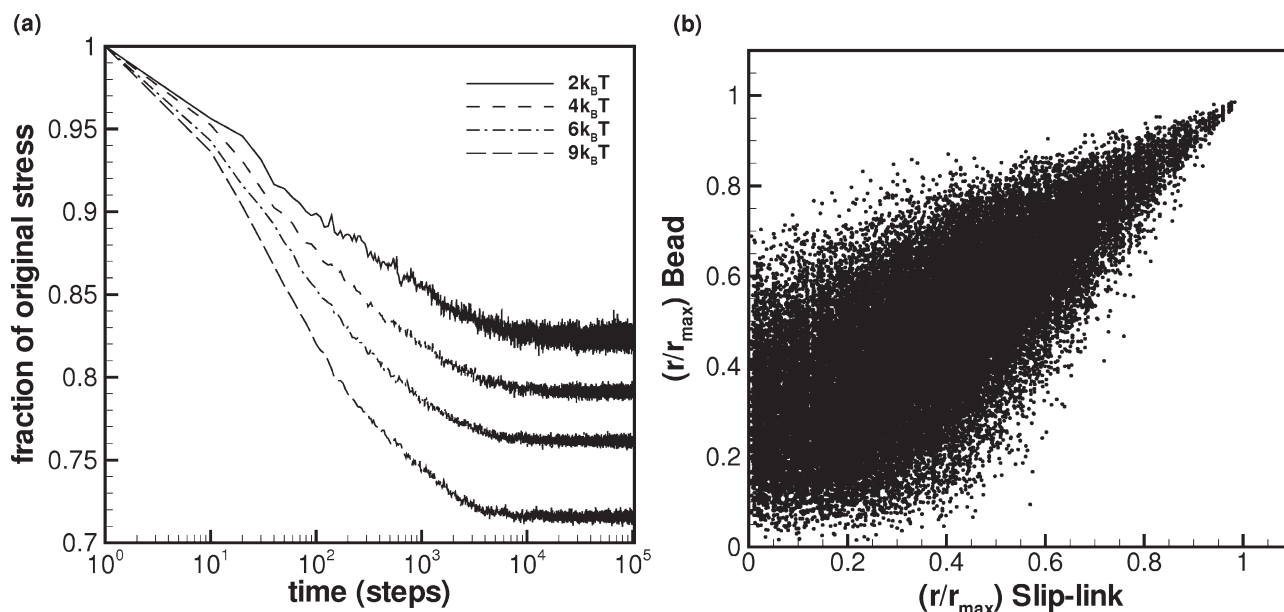
FIGURE 9 Scatter plots for the 125-bead simulation, annealed for 1000 time steps, and then subsequently stretched to stress levels per bond of (a) $2k_BT$, (b) $4k_BT$, (c) $6k_BT$, (d) $9k_BT$: each point represents a single pair of sliplinks in the simulation. The x-axis position is the total amount of chain between the sliplinks. The y-axis position is determined from the two sliplinks the bond lies between—it is their separation divided by their maximum separation.

pairs with an already large separation, r/r_{max}, in the stretch direction are brought close to their maximum separation. This is evident in Figure 9, where it is obvious that those pairs of sliplinks close to $r/r_{max} = 1$ are those with smaller lengths of chain between them—there is certainly a correlation between stretching and length of chain between sliplinks. This being said, it is interesting to note that it is not just sliplink pairs with one or two beads between them that are pulled tight. In Figure 9(d), one can observe sliplink pairs with over 10 beads separating them pulled tight.

There are certainly other projections of the data that could provide insight: for example, given that the initial orientation

of the sliplink pairs with respect to the applied strain (as well as their initial scalar separation) is clearly important, one could also correlate sliplink pair orientation with chain stretching. The three representations we have chosen are sufficient to demonstrate that bonds do become strongly stretched at the onset of strong strain hardening, and that there is some correlation with chains being pulled tight between entanglements.

A final question that might arise concerns the fraction of the stress which can be associated with chain orientation and stretching due to the entanglements. A simple way to test this, within the simulations, is to perform the deformation

FIGURE 10 (a) Fraction of stress remaining as a function of annealing time for the 125-bead simulation, annealed for 1000 time steps, and then subsequently stretched to stress levels per bond of $2k_BT$, $4k_BT$, $6k_BT$, $9k_BT$ and (finally) annealed without allowing chain motion through sliplinks. (b) Equivalent scatter plot to Figure 8, for the $9k_BT$ simulation after this annealing.

up to a given level of stress, and then to anneal the simulations at fixed strain, whilst switching off motion of the chain through the sliplinks. The fraction of stress remaining after the annealing is an indication of the fraction of stress due to the sliplinks. Figure 10 shows data taken from the 125-bead simulation, stretched by a factor of 4, annealed for 1000 time steps, and then subsequently stretched to stress levels of $2k_BT$, $4k_BT$, $6k_BT$, $9k_BT$ and finally annealed with chain motion through sliplinks switched off. Part (a) of the figure shows the stress relaxation during the final annealing, and indicates that a large fraction of the stress (70–85%) can be attributed to the sliplinks in this particular case. It is interesting to note here that the simulations with lower stress have a greater proportion of stress attributed to the sliplinks. This is a result of the particular deformation and annealing history of the simulation: the first annealing stage (1000 time steps) was sufficiently long so as to equilibrate chains between entanglements after the initial deformation. During the subsequent deformation, chain sections on lengthscales smaller than the entanglements begin to be deformed once more, giving nonentanglement contributions to the stress, so that the proportion of stress arising from the entanglements thus decreases with increasing strain.

Further confirmation that deformation of chain segments on lengthscales smaller than the entanglement length occurs is found by comparing the scatter plots in Figures 8(d) with 10(b), which show data immediately after stretching to a stress of $9k_BT$ per bond [Fig. 8(d)] and after annealing with chain motion through sliplinks frozen (10(b)). The main effect of this final annealing procedure is to remove all the points along the top of the scatter diagram, that is, to reduce the stretch of all springs close to their extension limit but not constrained to be so by sliplinks. Logically, this means that during the deformation up to $9k_BT$ per bond, these springs had become strongly stretched, not because of sliplink constraints but instead simply due to slow internal chain dynamics (i.e., the relaxation times of short lengthscale Rouse modes or glassy modes are longer than the stretch timescale).

We note that the simulations reported here represent quite an extreme case of deformation close to the extension limit for a material just below glass transition. Further below the glass transition, the chain dynamics are yet slower, and so an even smaller proportion of the hardening stress will be due to entanglements.

Our simulations, then, provide ample evidence to support the inferences drawn by Hine et al., that some chains are indeed pulled tight between entanglements at large strain, and that this appears to correlate with the transition from the weak to the strong strain hardening region. What is particularly notable, though, is that the majority of the chain segments do not do this: most are not pulled tight at all. To describe properly the behavior of the simulations, it is necessary to pay attention to the tails of the distribution, where the few strongly-stretched segments lie (whilst not ignoring the average behavior). Similar observations were made in simulations of strongly stretched polymer networks.[32] This is also reminiscent of the concept of "molecular individuality" introduced in the description of chain dynamics of dilute polymer solutions under extensional flow.[33,34] It presents a particular challenge to the development of constitutive models, where it is common to focus on the behavior of the "average" segment or to introduce some form of preaveraging: such an approach is bound to miss the effects of the tails of

the distribution. In our opinion this situation can only become worse when the entanglement molecular weight is lower (as is the case for most engineering thermoplastics) or as one probes temperatures further below the glass transition (where deformation becomes yet more local).

CONCLUSIONS

In conclusion, we have developed a simple bead-spring model, intended to mimic the internal dynamics of individual polymer chains in the region of the glass transition temperature. We have use this model to address the recent experiments of Hine et al.,[26] which investigated the effects of melt processing on stress-strain behavior. Samples were stretched, annealed at constant length for various times, then either subjected to shrinkage tests or further stress-strain tests. Our model reproduces, at a qualitative level, all the observations of Hine et al., namely (i) on annealing, the sample birefringence begins to drop immediately, for times shorter than the chain entanglement time, but (ii) the sample shrinkage remains constant up to about three times the entanglement time, dropping with a characteristic annealing timescale similar to the chain Rouse time, (iii) subsequent strain-hardening is reduced by even small amounts of annealing, and (iv) the strain-hardening curve appears to be correlated to sample shrinkage, such that curves for samples with the same shrinkage can be superposed by shifting along the strain axis. By detailed inspection of the simulation data, we were able to show that the a portion of the strain hardening could be attributed to deformation of chain substructures smaller than the entanglement length (note, in particular, the reduction in stress and change of chain configuration obtained by annealing the model at fixed strain, with entanglements fixed – as shown in Fig. 10). We also showed that the transition from the early, weaker strain hardening to the later, stronger, strain hardening was characterized by the pulling tight of a small fraction of chain segments trapped between entanglements (displayed in particular in the scatter plots of Figure 8, which correlate bond and entanglement stretching). The fact that it is just a small fraction of strands which give this behavior, (representing the tails of the distribution) is likely to pose a serious challenge towards constitutive modelling where it is common to focus on the behavior of the "average" segment or to introduce some form of preaveraging.

The fact that we were able to reproduce, at a qualitative level, the results of Hine et al., without optimization of the simulation parameters, suggests that the observations made may be quite general (i.e., that they do not depend sensitively on the choice of parameters). Exploration of a wider range of parameters would be required to confirm this; one possible exception is the limit of extensibility, determined by a combination of sliplink density and nonlinear spring parameters – not all models could be subjected to exactly the same strain and annealing history without over-extension.

To compare quantitatively with experimental data, it is clear that some optimization of parameters would be required. Additionally, since these simulations only consider the intramolecular spring forces (and their contribution to strain hard-

ening) one would need to add in the viscous, intermolecular contributions to the stress. At the simplest level, one might simply add a nonlinear viscous dashpot element to the stress obtained here (as in the models of refs. 1–6). However, there are already indications in the literature[9,13,14,18,20,21] of a viscous contribution to the hardening stress, which itself depends upon chain structure through the bond orientation. Since our simulations are primarily designed to approximate the chain dynamics in the glassy state, it would be possible to use them to infer the distribution of bond orientation following a complex strain-temperature history, which can then be used as an input to theories for viscous contributions to strain hardening. It is an interesting question as to whether our observations of superposition (or not) of strain-hardening curves would carry over to a new such theory or simulation in which viscous strain hardening is included. One factor suggesting that it may do so is that a signature of the strain hardening curves, relating to the issue of superposition, is the location of the crossover from weak to strong strain hardening; we may speculate that the location of this point would remain much the same if viscous contributions were added (as would occur, for example, if the viscous strain hardening were simply proportional to the intrachain stress that we calculate, or if it were just proportional to bond orientation). This, however, must remain for future investigation.

APPENDIX A: SPRING POTENTIALS

To develop the spring potentials, we consider a segment of chain containing fn inextensible monomer units. The FENE approximation to the spring potential for this is of form:

$$F(x,f) = -\frac{3}{2}Af \ln\left(1 - \frac{x^2}{f^2L^2}\right) + \frac{3}{2}\ln(fn) \qquad (A1)$$

The first term is the potential energy for extending the spring, and has the property that the maximum extension $x_{max} = fL$ where $L = nb$ is the maximum extension of a spring of n monomers each of length b. Near $x = 0$, the potential has the form $F \sim x^2/f$, which is the expected form for a Gaussian chain far from the extension limit. The second term in the potential energy provides a chemical potential for monomers if f is permitted to vary.

As indicated in the main text, we intend to use a potential of the form (A1) for each subspring (containing fn and $(1-f)n$ monomers respectively) either side of a sliplink. Supposing that the end-to-end vectors of the two springs are $\mathbf{x}_1$ and $\mathbf{x}_2$ such that:

$$\begin{aligned}\mathbf{x}_1 + \mathbf{x}_2 &= \mathbf{x} \\ \mathbf{x}_1 = (fx + \varepsilon, y, z), \ \mathbf{x}_2 &= ((1-f)x - \varepsilon, y, z)\end{aligned} \qquad (A2)$$
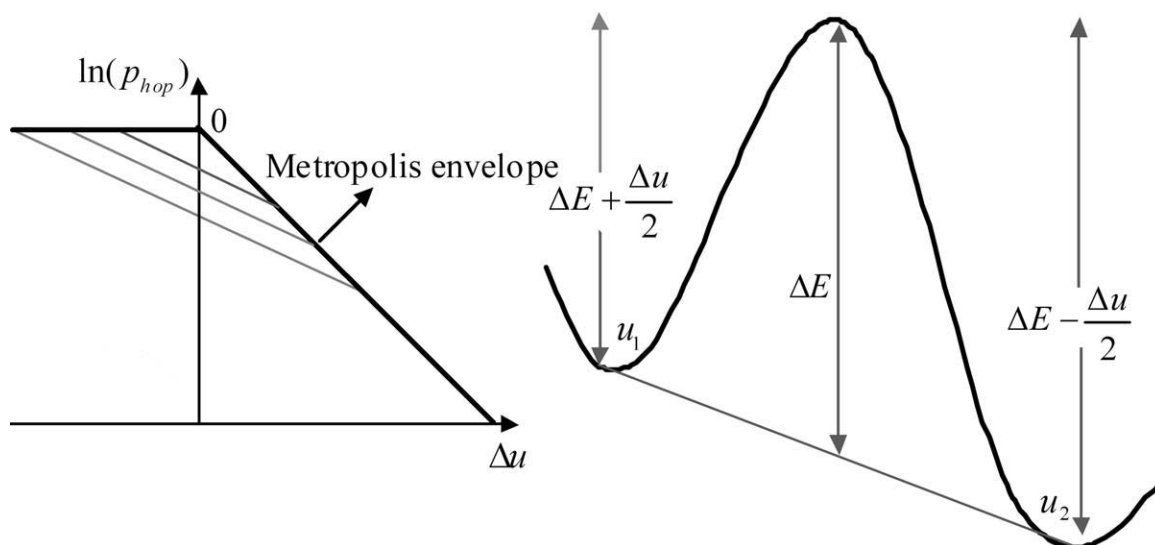
FIGURE 11 (Left) Schematic graph of acceptance probability as a function of energy change for different values of $p_0 \leq 1$. (Right) Schematic energy barrier that leads to hop acceptance criterion of eq B3.

then we may obtain a free energy for the combined chain of n monomers and end-to-end vector **x** via an integration over the sliplink position:

$$\exp\left(-F(x)\right) = \frac{1}{b^3} \int \exp(-F(x_1, f) - F(x_2, 1 - f)) d\varepsilon dy dz$$
(A3)

A saddle-point integral about the point $\varepsilon = y = z = 0$ yields

$$F(x) = -\left(\frac{3}{2}A + 2\right) \ln\left(1 - \frac{x^2}{L^2}\right) + \frac{1}{2}\ln\left(1 + \frac{x^2}{L^2}\right) + \frac{3}{2}\ln n$$
(A4)

which is equivalent to eq 1 with $\alpha = A + \frac{4}{3}$. This is the form of potential we use for the springs without sliplinks. For the springs with sliplinks, we use the form (A1) but modified appropriately for the case of f close to 0 or 1, where the saddle point integration breaks down. These modifications are briefly described in the main text.

APPENDIX B: MONTE-CARLO HOP ACCEPTANCE CONDITIONS

For simulation of chain dynamics we use a dynamic Monte Carlo scheme, based on the principle of detailed balance. As is standard in such schemes, a trial change of state of the system (e.g., a change in a bead position) is generated randomly, and the trial move accepted with a certain probability based on the change of energy. Detailed balance requires that (all other factors being equal) the probability p_{12} of accepting a change from state 1 to state 2 is related to the probability p_{21} of accepting the reverse change (state 2 to state 1) via

$$p_{12} = p_{21} \exp(-\Delta u_{12})$$

where Δu_{12} is the change in energy from state 1 to state 2. Given this constraint, there remains some freedom in speci-

fying how p_{12} is related to Δu_{12}. The Metropolis scheme[30] specifies

$$p_{12} = \text{Min}\left[\exp\left(-\Delta u_{12}\right), 1\right]$$
(B1)

and is designed to give the fastest possible exploration of phase space consistent with detailed balance. It does not, however, correspond to any physically realisable dynamics.

An alternative is to use

$$p_{12} = \frac{\exp\left(-\Delta u_{12}\right)}{1 + \exp\left(-\Delta u_{12}\right)}$$
(B2)

which is slower in exploring phase space by (roughly) a factor of 2. Equation B2 can be derived by assuming a process such that, once a trial change from state 1 to state 2 is chosen, the system is allowed to equilibrate between state 1 and state 2 and then decide between them based on their relative Boltzmann probabilities. This could by physically realized by having an uncrossable barrier between the two states which is removed for a sufficiently long time that the system then explores both states many times. The barrier is then replaced, fixing the system in either state 1, in which case there is no change of state, or in state 2, which occurs with probability B2.

A third option is

$$p_{12} = \text{Min}\left[\exp\left(-\Delta u_{12}\right), p_0 \exp\left(-\Delta u_{12}/2\right), 1\right].$$
(B3)

This satisfies detailed balance, because in the region where $p_{12} = p_0 \exp(-\Delta u_{12}/2)$, the probability for the reverse hop is $p_{21} = p_0 \exp(-\Delta u_{21}/2) = p_0 \exp(\Delta u_{12}/2)$, and so $p_{12} = p_{21} \exp(-\Delta u_{12})$ as required. This dependence of p_{12} on Δu_{12} is illustrated in Figure 11 for a range of values of $p_0 \leq 1$. When $p_0 = 1$, the Metropolis scheme is recovered, but for smaller p_0 the probability of acceptance is suppressed for state

changes with small energy difference ($|\Delta u_{12}| < 2 \ln p_0$). Within this region, this can be thought of as approximating the physical dynamics arising from of activated changes of state occurring via traversal of large energy barriers. If we suppose there was (in reality) an energy barrier of average height ΔE between the states 1 and 2 (as illustrated in Fig. 11) then standard transition state theory dictates that the rates of transition between state 1 and 2 should follow

$$\text{rate}\,(1 \to 2) = A \exp\left(-\Delta E - \Delta u_{12}/2\right) \sim p_0 \exp\left(-\Delta u_{12}/2\right)$$
$$\text{rate}\,(2 \to 1) = A \exp\left(-\Delta E - \Delta u_{21}/2\right) \sim p_0 \exp\left(-\Delta u_{21}/2\right)$$

Hence, the region of eq B3 where $p_{12} = p_0 \exp(-\Delta u_{12}/2)$ approximates the dynamics in the physical situation where energy barriers in the system are of a "typical" height ΔE. In this case we would expect changes of state with negative energy difference ($\Delta u_{12} \ll 0$) to be accelerated relative to those with small energy difference ($\Delta u_{12} \approx 0$), because (as shown in Fig. 11) the energy landscape is tilted and the energy barrier from state 1 to state 2 reduced (conversely, the barrier is increased from state 2 to state 1). It is this feature that eq B3 approximates, at least within the range ($|\Delta u_{12}| < 2 \ln p_0$).

REFERENCES AND NOTES

1 Arruda, E. M.; Boyce, M. C. *Int. J. Plast.* **1993,** *9*, 697–720.

2 Boyce, M. C.; Parks, D. M.; Argon, A. S. *Mech. Mater.* **1988,** *7*, 15–33.

3 Wu, J. J.; Buckley, C. P. *J. Polym. Sci. Part B: Polym. Phys.* **2004,** *42*, 2027–2040.

4 Buckley, C. P.; Jones, D. C. *Polymer* **1995,** *36*, 3301–3312.

5 Klompen, E. T. J.; Engels, T. A. P.; Govaert, L. E.; Meijer, H. E. H. *Macromolecules* **2005,** *38*, 6997–7008.

6 Govaert, L. E.; Tervoort, T. A. *J. Polym. Sci. Part B: Polym. Phys.* **2004,** *42*, 2041–2049.

7 Kramer, E. J. *J. Polym. Sci. Part B: Polym. Phys.* **2005,** *43*, 3369–3371.

8 van Melick, H. G. H.; Govaert, L. E.; Meijer, H. E. H. *Polymer* **2003,** *44*, 2493–2502.

9 Wendlandt, M.; Tervoort, T. A.; van Beek, J. D.; Suter, U. W. *J. Mech. Phys. Solids* **2006,** *54*, 589–610.

10 Rossle, W.; Lindner, P.; Dettenmaier, M. *Physica B* **1989,** *156*, 414–416.

11 Dettenmaier, M.; Maconnachie, A.; Higgins, J. S.; Kausch, H. H.; Nguyen, T. Q. *Macromolecules* **1986,** *19*, 773–778.

12 Casas, F.; Alba-Simionesco, C.; Montes, H.; Lequeux, F. *Macromolecules* **2008,** *41*, 860–865.

13 Hoy, R. S.; Robbins, M. O. *Phys. Rev. Lett.* **2007,** *99*, 117801.

14 Hoy, R.S.; Robbins, M. O. *Phys. Rev. E.* **2008,** *77*, 31801.

15 Hoy, R. S.; Robbins, M. O. *J. Chem. Phys.* **2009,** *131*, 244901.

16 Li, J.; Mulder, T.; Vorselaars, B.; Lyulin, A. V.; Michels, M. A. J. *Macromolecules* **2006,** *39*, 7774–7782.

17 Chui, C.; Boyce, M. C. *Macromolecules* **1999,** *32*, 3795–3808.

18 Chen, K.; Schweizer, K. S. *Phys. Rev. Lett.* **2009,** *102*, 038301.

19 Hasan, O. A.; Boyce, M. C. *Polymer* **1993,** *34*, 5085–5092.

20 Senden, D. J. A.; Van Dommelen, J. A. W.; Govaert, L. E. *J. Polym. Sci. Part B: Polym. Phys.* **2010,** *48*, 1483–1494.

21 Ge, T.; Robbins, M. O. *J. Polym. Sci. Part B: Polym. Phys.* **2010,** *48*, 1473–1482.

22 Bent, J.; Hutchings, L. R.; Richards, R. W.; Gough, T.; Spares, R.; Coates, P. D.; Grillo, I.; Harlen, O. G.; Read, D. J.; Graham, R. S.; Likhtman, A. E.; Groves, D. J.; Nicholson, T. M.; McLeish, T. C. B. *Science* **2003,** *301*, 1691–1695.

23 Collis, M. W.; Lele, A. K; Mackley, M. R.; Graham, R. S.; Groves, D. J.; Likhtman, A. E.; Nicholson, T. M.; Harlen, O. G.; McLeish, T. C. B.; Hutchings, L. R.; Fernyhough, C. M.; Young, R. N. *J. Rheol.* **2005,** *49*, 501–522.

24 Doi, M.; Edwards, S. F. The Theory of Polymer Dynamics; Clarendon: Oxford, **1986.**

25 McLeish, T. C. B. *Adv. Phys.* **2002,** *51*, 1379–1527.

26 Hine, P. J.; Duckett, A.; Read, D. J. *Macromolecules* **2007,** *40*, 2782–2790.

27 Doi, M.; Takimoto, J. *Philos. Trans. R. Soc. London, Ser. A* **2003,** *361*, 641–650.

28 Schieber, J. D.; Neergaard, J.; Gupta, S. *J. Rheol.* **2003,** *47*, 213–233.

29 Likhtman, A. E. *Macromolecules* **2005,** *38*, 6128–6139.

30 Metropolis, N.; Rosenbluth, A. W.; Rosenbluth, M. N.; Teller, A. H. *J. Chem. Phys.* **1953,** *21*, 1087–1092.

31 Lyhne, A.; Rasmussen, H. K.; Hassager, O. *Phys. Rev. Lett.* **2009,** *102*, 138301.

32 Everaers, R. *New J. Phys.* **1999,** *1*, 12.1–12.53.

33 Perkins, T. T.; Smith, D. E.; Chu, S. *Science* **1997,** *276*, 2016–2021.

34 Masubuchi, Y.; Furuichi, K.; Horio, K. *J. Chem. Phys.* **2009,** *131*, 114906.